BIOCHEMISTRY
including biophysical chemistry & molecular biology

ARTICLE

pubs.acs.org/biochemistry

Characterization of Dye-Decolorizing Peroxidases from *Rhodococcus jostii* RHA1

Joseph N. Roberts,[†] Rahul Singh,[†] Jason C. Grigg,[†] Michael E. P. Murphy,[†] Timothy D. H. Bugg,[‡] and Lindsay D. Eltis*[,†]

[†]Department of Microbiology and Immunology, University of British Columbia, 2350 Health Sciences Mall, Vancouver, British Columbia V6T 1Z3, Canada

[‡]Department of Chemistry, University of Warwick, Coventry CV4 7AL, U.K.

Supporting Information

ABSTRACT: The soil bacterium *Rhodococcus jostii* RHA1 contains two dye-decolorizing peroxidases (DyPs) named according to the subfamily they represent: DypA, predicted to be periplasmic, and DypB, implicated in lignin degradation. Steady-state kinetic studies of these enzymes revealed that they have much lower peroxidase activities than C- and D-type DyPs. Nevertheless, DypA showed 6-fold greater apparent specificity for the anthraquinone dye Reactive Blue 4 (k_{cat}/K_m = 12800 ± 600 M^{-1} s^{-1}) than either ABTS or pyrogallol, consistent with previously characterized DyPs. By contrast, DypB showed the greatest apparent specificity for ABTS (k_{cat}/K_m = 2000 ± 100 M^{-1} s^{-1}) and also oxidized Mn^{II} (k_{cat}/K_m = 25.1 ± 0.1 M^{-1} s^{-1}). Further differences were detected using electron paramagnetic resonance (EPR) spectroscopy: while both DyPs contained high-spin (S = $^5/_2$) Fe^{III} in the resting state, DypA had a rhombic high-spin signal (g_y = 6.32, g_x = 5.45, and g_z = 1.97) while DypB had a predominantly axial signal (g_y = 6.09, g_x = 5.45, and g_z = 1.99). Moreover, DypA reacted with H_2O_2 to generate an intermediate with features of compound II (Fe^{IV}=O). By contrast, DypB reacted with H_2O_2 with a second-order rate constant of (1.79 ± 0.06) × 10^5 M^{-1} s^{-1} to generate a relatively stable green-colored intermediate ($t_{1/2}$ ~ 9 min). While the electron absorption spectrum of this intermediate was similar to that of compound I of plant-type peroxidases, its EPR spectrum was more consistent with a poorly coupled protein-based radical than with an [Fe^{IV}=O Por$^{\bullet}$]$^+$ species. The X-ray crystal structure of DypB, determined to 1.4 Å resolution, revealed a hexacoordinated heme iron with histidine and a solvent species occupying axial positions. A solvent channel potentially provides access to the distal face of the heme for H_2O_2. A shallow pocket exposes heme propionates to the solvent and contains a cluster of acidic residues that potentially bind Mn^{II}. Insight into the structure and function of DypB facilitates its engineering for the improved degradation of lignocellulose.

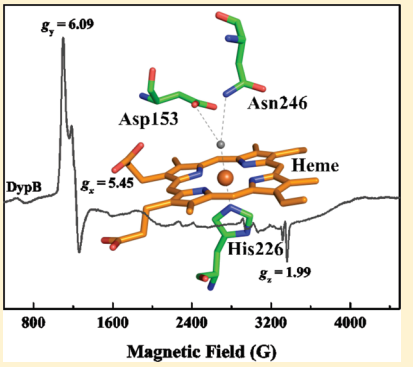

The dye-decolorizing peroxidases (DyPs) were first recognized a mere decade ago when DyP_{Dec1} was isolated from the fungus *Thanatephorus cucumeris* Dec1 for their ability to degrade anthraquinones (AQs), a class of dyes that are widely used by the textile industry.[1] Genomic analyses have since revealed that DyPs occur in a wide range of fungi and bacteria.[2] Similar to plant-type peroxidases, DyPs contain a heme prosthetic group. However, structural analyses have revealed that DyPs have a ferredoxin-like fold similar to that of chlorite dismutase and thus belong to a different superfamily than the plant-type peroxidases.[3] Phylogenetic analyses have led to the classification of DyPs into four subfamilies (A−D).[4] In addition to AQ dyes, these enzymes exhibit peroxidase activity toward carotenoids, methoxylated aromatics such as veratryl alcohol, lignin model compounds, and more typical peroxidase substrates such as 2,2′-azinobis(3-ethylbenzthiazoline-6-sulfonic acid) (ABTS).[5−9]

The physiological role of DyPs remains unclear. Consistent with their peroxidase activity, DyPs have been thought to be part of the bacterial oxidative stress response based on the co-induction of a DyP with structural components of gas vesicles during oxidative stress.[10] Similarly, DyPs have been proposed to act as virulence factors in plant pathogens on the basis of their ability to kill plant cells and to wilt seedlings.[11] However, recent molecular genetic evidence suggests that in *Escherichia coli*, A-type DyPs assist in capturing iron from heme while keeping the tetrapyrrole skeleton intact.[12] Intriguingly, some B-type DyPs occur within icosohedral shells formed by encapsulin, a protein that is also predicted to compartmentalize some bacterial ferritin-like proteins.[13] It is possible that the different subfamilies of DyPs have different physiological roles.

The catalytic mechanism of DyPs has been proposed to be similar to that of plant-type peroxidases.[2,3] Accordingly, the ferric enzyme reacts with H_2O_2 to yield compound I, a high-valent intermediate designated [Fe^{IV}=O Por$^{\bullet}$]$^+$ that is two reducing

Received: November 29, 2010
Revised: April 28, 2011
Published: May 02, 2011

equivalents more oxidized than the resting ferric enzyme. Compound I reacts with 1 equiv of the reducing substrate to yield an $[Fe^{IV}{=}O]$ intermediate called compound II. Reaction with a second equivalent of the reducing substrate yields the resting-state Fe^{III} peroxidase. Nevertheless, the few mechanistic and structural studies of DyPs indicate important differences with the plant-type peroxidases. For example, the reaction of DyP_{Dec1} with H_2O_2 yielded a species with a half-life of ~9 min that was assigned as an unusually stable $[Fe^{IV}{=}O\ Por^{\bullet}]^{+}$ and slowly decays to the ferric enzyme with no detectable compound II-type intermediate.[2,3,14,15] Moreover, although the heme is ligated by a proximal histidine that forms a hydrogen bond with a conserved acidic residue in both classes of peroxidases, the residues on the distal face of the heme differ.[3,16] Thus, DyPs have a conserved aspartate and arginine on the distal face. The former replaces the catalytic histidine of plant-type peroxidases and, on the basis of the reduced reactivity of the D171N variant of DyP_{Dec1} toward H_2O_2,[3] has been proposed to shuttle a proton in the formation of compound I from H_2O_2, analogous to the distal glutamate of chloroperoxidase (CPO). For its part, the arginine has been proposed to stabilize the negative charge on the distal oxygen of the Fe-bound peroxide during O−O bond cleavage,[2] as proposed by Poulos and Kraut.[17] However, this role has not been substantiated experimentally. More extensive structure−function studies of DyPs, particularly involving electron paramagnetic resonance (EPR) and stopped-flow absorption spectroscopies, are required to investigate their catalytic mechanism and to elucidate the roles of active site residues.

Rhodococcus is a genus of catabolically versatile soil bacteria that belong to a mycolic acid-containing suborder of actinobacteria.[18] The ability of rhodococci to transform a wide range of organic compounds and pollutants, combined with their robust growth and exceptional stress tolerance, has led to their use in a wide range of biotechnological applications.[19] *Rhodococcus jostii* RHA1 was isolated from lindane-contaminated soil and was initially characterized for its potent PCB (polychlorinated biphenyl)-degrading properties.[20] Subsequent genomic studies of RHA1 have provided important insights into the physiology and catabolic versatility of rhodococci and related actinobacteria.[21] Most recently, we demonstrated that RHA1 can degrade lignin and lignocellulose, producing a number of monocyclic phenolic compounds.[22] This is consistent with RHA1's ability to degrade a wide range of such aromatic compounds.[18,21] Molecular genetic and biochemical studies have demonstrated that this ability to degrade lignin depends on DypB, one of two DyPs that RHA1 harbors (DOI 10.1021/bi101892z). A second DyP, DypA, is predicted to occur in the periplasm and is a homologue of EfeB, which has been implicated in iron uptake in *E. coli*.[12] Like *efeB*, *dypA* occurs in an operon with other genes predicted to be involved in iron uptake intact.

Herein, we describe the biochemical characterization of the two RHA1 DyPs. We investigated the specificity of these enzymes for a range of organic substrates as well as the enzymes' reactivities with H_2O_2. The ferric-heme environment in the two enzymes was characterized using EPR spectroscopy, which was further used in combination with stopped-flow absorption spectroscopy to investigate the catalytic intermediates in DypB. We further provide kinetic and spectroscopic evidence of manganese peroxidase activity in DypB. Finally, the X-ray crystal structure of DypB was determined, providing insight into substrate access and putative active site residues. The results are discussed with respect to the reactivity and catalytic mechanism of DyPs and plant-type peroxidases.

MATERIALS AND METHODS

Reagents and Chemicals. HPLC-grade DMSO was from Alfa Aesar. All other reagents and chemicals were purchased from SIGMA-Aldrich, ACROS, MP Biomedicals, or Fisher and were used without further purification. Water was purified using a Barnstead NANOpure UV apparatus (Barnstead International, Dubuque, IA) to a resistivity of greater than 17 MΩ cm.

Protein Analysis. Protein concentrations were measured using the Micro BCA assay (Thermo Scientific). The heme concentration was determined using a pyridine hemochromogen assay.[23]

Spectroscopy. A Cary 5000 spectrophotometer (Varian) equipped with a thermostated cuvette holder maintained at 25.0 ± 0.5 °C was used to record electronic absorption spectra and to monitor steady-state kinetics. The 9 GHz EPR spectra were recorded using a Bruker ER500 spectrometer equipped with a standard TE_{102} cavity, a liquid helium cryostat (Oxford Instruments), and a microwave frequency counter (Bruker ER049X). EPR spectra representing four scans were recorded for 200 μL solutions of 0.1 mM ferric DyP in 20 mM MOPS and 80 mM NaCl (pH 7.5) contained in a 4 mm diameter EPR tube. Samples were frozen in liquid N_2. After spectra of ferric DypB had been recorded, the sample was thawed, mixed on ice with 2 μL of 2 mM H_2O_2 (~2 s), and rapidly immersed in liquid N_2. The spectra of the ferric enzyme and the sample containing DypB reacted with H_2O_2 were recorded at 5 K using a 5 G modulation amplitude, a 1 mW microwave power, and a 100 kHz modulation frequency. The temperature dependence of the radical was similarly measured except that the temperature was varied from 5 to 20 K and two scans were taken at each temperature. For the spectrum of the radical centered at $g = 2$, recorded at 40 K, six scans were taken using a 0.5 G modulation amplitude, a 0.1 mW microwave power, and a 100 kHz modulation frequency.

Steady-State Kinetic Analysis. Steady-state reaction kinetics were monitored spectrophotometrically. The standard assay was performed in 1 mL of 50 mM sodium acetate (pH 4.5) at 25.0 ± 0.5 °C containing 10 mM ABTS, 1.0 mM H_2O_2, and the appropriate amount of DyP. Reactions were initiated with the addition of H_2O_2, and initial rates were monitored at 414 nm (ε_{414} = 36.6 mM^{-1} cm^{-1}[24]).

Apparent steady-state kinetic parameters were evaluated for ABTS, pyrogallol (1,2,3-trihydroxybenzene), Reactive Blue 4 (RB4), and $MnSO_4$ using 1.0 mM H_2O_2 and the following wavelengths for each of the last three reductants: 430 nm (ε_{430} = 2.47 mM^{-1} cm^{-1}[25]), 610 nm (ε_{610} = 4.2 mM^{-1} cm^{-1}[26]), and 270 nm (ε_{270} = 11.59 mM^{-1} cm^{-1}[27]). Reactions with ABTS (1.0−40 mM), pyrogallol (0.1−20 mM), and RB4 (0.1−0.6 mM) were performed using 50 mM sodium acetate (pH 4.5). Reactions with 1−20 mM $MnSO_4$ were performed using 50 mM sodium malonate (pH 4.5) as described previously.[27] Kinetic parameters were evaluated for H_2O_2 at 10 mM ABTS, 20 mM pyrogallol, 5 mM RB4, and 17.5 mM $MnSO_4$. Steady-state kinetic equations were fit to the data using LEONORA.[28]

Stopped-Flow Kinetics. Transient-state kinetics were performed using an SX18 stopped-flow spectrophotometer (Applied PhotoPhysics Ltd.) equipped with a diode array detector and a monochromator. A circulating water bath was used to maintain the temperature of the reactant syringes and the mixing cell at 25 °C. Typically, 10 μM enzyme (heme) was mixed with an equal volume of H_2O_2 at various concentrations at pH 4.5 and 7.5. Multiwavelength data were analyzed using

Table 1. X-ray Diffraction Data Collection and Refinement Statistics

	SeMet-DypB				
	peak	inflection	remote	DypB ($P3_221$)	DypB ($R32/H32$)
			Data Collection[a]		
wavelength (Å)	0.97882	0.97904	0.97692	0.97949	1.00000
resolution range (Å)	48.5−2.6 (2.74−2.60)	48.5−2.6 (2.74−2.60)	48.5−2.6 (2.74−2.60)	48.4−2.25 (2.37−2.25)	33.93−1.40 (1.48−1.40)
space group	$P3_221$	$P3_221$	$P3_221$	$P3_221$	$H32$
unit cell dimensions (Å)	a = 132.7, b = 132.7, c = 160.6	a = 132.7, b = 132.7, c = 160.6	a = 132.7, b = 132.7, c = 160.7	a = 132.3, b = 132.3, c = 160.2	a = 127.7, b = 127.7, c = 178.2
no. of unique reflections	50808	50861	50840	77338	108171
completeness (%)	100 (100)	100 (100)	100 (100)	100 (100)	98.9 (96.2)
average $I/\sigma I$	43.2 (12.3)	41.0 (9.1)	37.9 (6.7)	14.2 (2.6)	16.3 (3.3)
redundancy	11.2 (11.4)	11.2 (11.4)	11.2 (11.4)	5.7 (4.5)	6.1 (5.3)
R_{merge}	0.039 (0.201)	0.044 (0.290)	0.052 (0.402)	0.073 (0.577)	0.049 (0.387)
Wilson B (Å^2)	58.6	57.2	57.3	46.8	13.8
			Refinement		
R_{work} (R_{free})	–	–	–	19.2 (21.8)	13.0 (14.7)
B factor (Å^2)	–	–	–		
all atoms	–	–	–	41.7	16.2
protein	–	–	–	41.6	14.4
heme	–	–	–	32.3	10.5
water	–	–	–	42.7	27.1
rmsd for bond lengths (Å)	–	–	–	0.013	0.012
% in most favorable region	–	–	–	91.9	91.3
% in disallowed regions	–	–	–	0.1	0.0
PDB entry	–	–	–	3QNR	3QNS

[a] Values in parentheses represent data for the highest-resolution shell.

dx.doi.org/10.1021/bi200427h |*Biochemistry* 2011, 50, 5108–5119

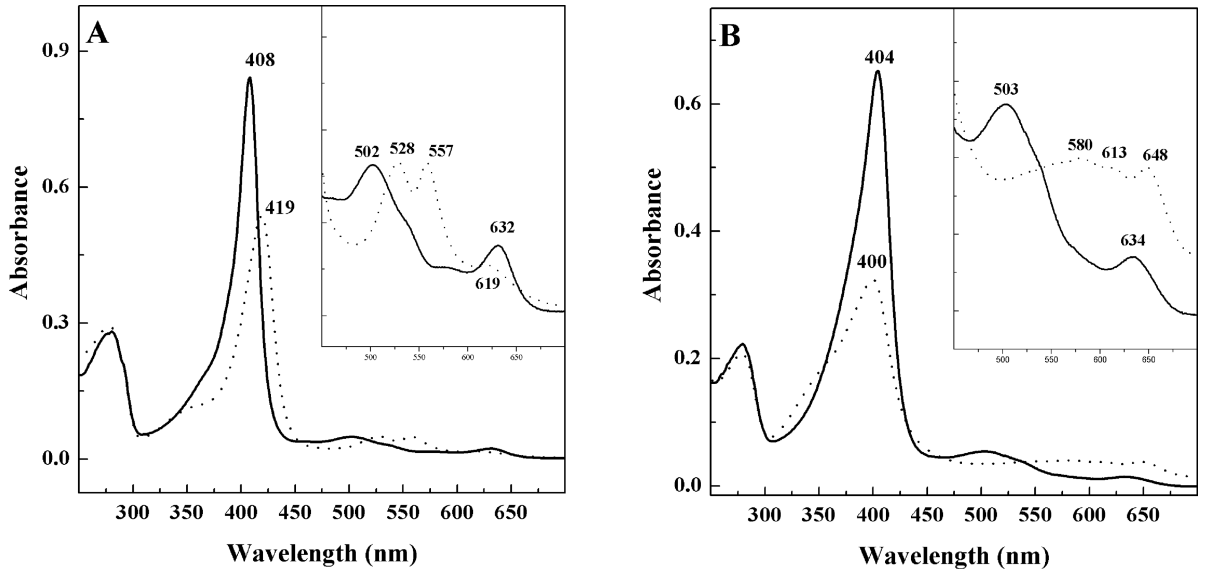

Figure 1. Electronic absorption spectra of DypA (A) and DypB (B). The samples contained 10 μM ferric enzyme (—) or the same sample with 10 μM H_2O_2 (···) in 20 mM MOPS and 80 mM NaCl (pH 7.5, 25 °C).

singular-value decomposition (SVD) with Pro-K.2000 Global Analysis (Applied PhotoPhysics) to obtain the transition rates (k_n) between intermediates. Reactions were then monitored at selected single wavelengths to follow the formation and decay of intermediates, and the data were fitted using multiple-exponential equations to obtain pseudo-first-order rate constants (k_{obs}). Second-order rate constants for the formation of compound I were evaluated from plots of k_{obs} versus H_2O_2 concentration.

Determination of DypB Structure. Selenomethionine-labeled DypB was prepared as previously described[29] and purified as described for the unlabeled protein (DOI 10.1021/bi101892z). Heme-bound DypB crystals were grown by hanging drop vapor diffusion at room temperature. Drops were made from 2 μL of an 18 mg/mL protein solution in 20 mM MOPS (pH 7.5), 80 mM NaCl, and 2 μL of well solution. The well solution for the selenomethionine-labeled and native primitive trigonal ($P3_221$) crystal form contained 3.5 M sodium formate (pH 7.5), and crystals formed overnight. The well solution for the native rhombohedral ($R32$) crystal form contained 1.26 M ammonium sulfate and 0.1 M HEPES (pH 7.5) and crystals grew over the course of 3 months. To prepare crystals for mounting, they were briefly soaked in well solution supplemented with 16% glycerol and then flash-frozen by immersion in liquid nitrogen.

X-ray diffraction data of the $P3_221$ crystal forms were collected at the Canadian Light Source on beamline 08ID-1. Multiple-wavelength anomalous diffraction data from selenomethionine-labeled DypB were collected at wavelengths of 0.97882 (peak), 0.97904 (inflection), and 0.97692 Å (remote). Native diffraction data were collected at a wavelength of 0.97955 Å. Data were processed using XDS[30] and scaled using Scala.[31] Solve[32] and Resolve[33,34] were used to obtain phases from the 15 identified selenium sites and to build a preliminary model. The phase solution had an initial figure of merit of 0.66 that was improved to 0.74 by density modification. The structure was manually edited using Coot[35] and refined using translation libration screw (TLS) parameters[36] with Refmac5[37] from the CCP4 program suite.[38] The native structure was refined to 2.1 Å resolution and contained three DypB molecules in the asymmetric unit.

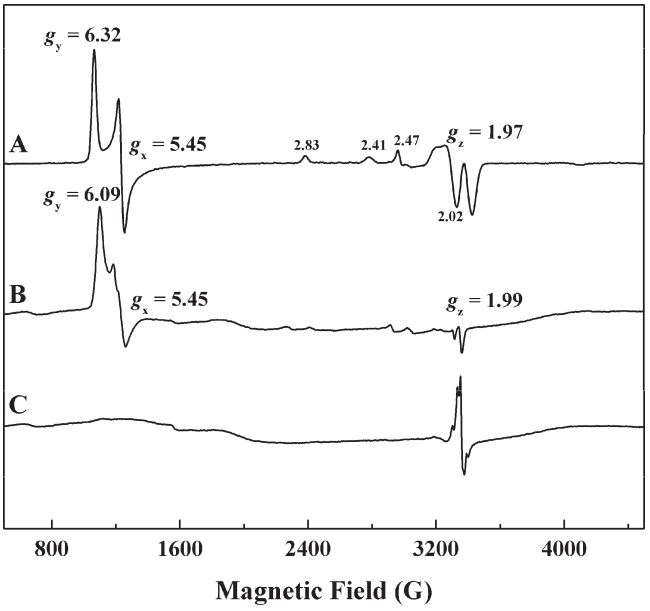

Figure 2. EPR spectra of DypA and DypB. Samples contained 0.1 M (A) ferric DypA, (B) ferric DypB, or (C) DypB incubated for ~2 s in the presence of 2 mM H_2O_2 [20 mM MOPS and 80 mM NaCl (pH 7.5)]. Spectra were recorded at 5 K using a 9 GHz spectrometer.

Diffraction data for the $R32$ crystal form were collected at the Stanford Synchrotron Radiation Laboratory on beamline 7-1 at a wavelength of 1.0000 Å. Data were processed and scaled using Mosflm[39] and Scala,[31] respectively. The structure was determined by molecular replacement using a single protein chain from the $P3_221$ structure as a search model in MolRep.[40] The structure was edited using Coot[35] and refined as the equivalent space group $H32$ with Refmac5.[37] The structure was refined to 1.4 Å resolution and contained one DypB molecule in the asymmetric unit. The final model includes one DypB protamer (residues 6−313), two molecules of glycerol, two molecules of

Table 2. Steady-State Kinetic Parameters of DypA and DypB from RHA1[a]

		reducing substrate			H_2O_2		
	Dyp	K_m (mM)	k_{cat} (s^{-1})	k_{cat}/K_m (M^{-1} s^{-1})	K_m (μM)	k_{cat} ($\times 10^{-3}$ s^{-1})	k_{cat}/K_m ($\times 10^3$ M^{-1} s^{-1})
ABTS	A	8.2 (0.5)	16.83 (0.04)	2000 (100)	4100 (200)	68000 (2000)	16.8 (0.5)
	B	23 (2)	55 (2)	2400 (100)	67 (3)	14100 (200)	210 (8)
pyrogallol	A	9.9 (1.3)	0.49 (0.03)	50 (3)	640 (40)	310 (10)	0.49 (0.03)
	B	5.7 (0.4)	3.4 (0.1)	600 (20)	30 (1)	2080 (40)	79 (2)
RB4	A	1 (0.2)	13 (2)	12800 (600)	48 (2)	4900 (40)	102 (3)
	B	0.35 (0.05)	0.050 (0.003)	140 (10)	6.4 (0.9)	21.5 (0.6)	3.4 (0.4)
Mn^{II}	B	24 (2)	0.59 (0.04)	25.1 (0.1)	1.3 (0.2)	17600 (500)	134 (2)

[a] Values in parentheses represent the standard error.

sulfate, and 409 water molecules. Relative to the peptide sequence,[21] the crystal structure is missing 5 and 37 residues at the N- and C-termini, respectively. More than 92.1% of the ϕ and ψ angles fall within the most favorable regions of Ramachandran plots, and none are in the disallowed regions. Data collection and refinement statistics are listed in Table 1. Structure figures were generated with PYMOL (DeLano Scientific, San Carlos, CA). The native $P3_221$ and $R32$ structures were considered identical with a root-mean-square deviation (rmsd) of superimposed Cα atoms of 0.24 Å and a TM score of 1. All analysis and figures were generated from the coordinates derived from the higher-resolution $R32$ space group.

RESULTS

Electronic Structure of Ferric DypA and DypB. As noted in the preceding paper (DOI 10.1021/bi101892z), neither recombinant DyP contained detectable amounts of heme when purified from *E. coli*. However, both could be stably reconstituted with heme. The electronic structures of ferric DypA and DypB were analyzed using electronic absorption and EPR spectroscopies. The electronic absorption spectra of ferric DypA (Figure 1A, solid line) and DypB (Figure 1B, solid line) showed distinct spectral features. In DypA, these features were sharper, with a Soret band at 408 nm and charge transfer bands, CT1 and CT2, at 632 and 502 nm, respectively. By contrast, the Soret band of DypB was at 404 nm with a shoulder at ~360 nm and visible features at 634 and 503 nm. Using a pyridine−hemochrome assay, the molar absorption coefficients of reconstituted DypA and DypB were 126 mM^{-1} cm^{-1} (ε_{408}) and 84 mM^{-1} cm^{-1} (ε_{404}) (Figure S1 of the Supporting Information). The *Rz* values of DypA and DypB were 2.7 and 2.9, respectively. These values did not change significantly upon storage of protein solutions for up to 6 months at −80 °C or for 24 h at 4 °C

EPR spectroscopy of the ferric enzymes provided further insight into the heme microenvironment of DypA and DypB. At 5 K, the 9 GHz EPR spectrum of ferric DypA (Figure 2A) predominantly comprised a rhombically distorted ($g_x \neq g_y$) axial resonance at $g_\perp \approx 6$ (g_y = 6.32, g_x = 5.45, and g_z = 1.97). The resonance between g = 3 and g = 2 further suggests the presence of a significant proportion of low-spin heme in the reconstituted protein. For DypB (Figure 2B), the major resonance was axial at $g_\perp \approx 6$ with a slightly resolved rhombic feature (g_y = 6.09, and g_x = 5.45) and $g_\parallel$ = 1.97. The absolute difference in g values ($\Delta g = g_y - g_x$) at g = 6 was used to calculate the percentage of rhombicity, R ($R = \Delta g/16 \times 100\%$), in the major DyP species.[41] The Δg values for DypA and DypB were calculated to be 0.87 and 0.65, respectively, yielding R values of 5.44% for DypA and 4.06% for DypB. Overall, the spectra indicate that both DypA and DypB predominantly contain high-spin Fe^{III}, although the differences in the spectra suggest different coordination microenvironments for the heme iron in the two paralogues.

Apparent Substrate Specificities of DyPs. Using ABTS as a substrate, the optimal pH values of the reactions with DypA and DypB were 3.5 and 4, respectively (results not shown). For DypB, the activity at pH 7.5 was 1% of that at pH 4. For DypA, the activity was not detected at pH >6. As DypB precipitated below pH 4.0, 50 mM acetate (pH 4.5) was used in subsequent experiments. Reactions involving ABTS were corrected for the nonenzymatic reaction of this compound with H_2O_2. In the standard assay, the nonenzymatic increase in A_{414} accounted for 32% of the total rate observed in the presence of DypA and 11% of the rate in the presence of DypB. Both DyPs oxidized ABTS, pyrogallol, and RB4 in an H_2O_2-dependent fashion under steady-state conditions. DypB was also found to oxidize Mn^{II} in an H_2O_2-dependent fashion in the presence of 50 mM malonate (pH 4.5), as indicated by an increase in absorbance at 270 nm (Figure S2 of the Supporting Information). The oxidation of Mn^{II} was also observed using a previously described assay[42] involving 20 mM HEPES (pH 7.6) and 0.5 mM pyrophosphate (results not shown).

In the presence of 1 mM H_2O_2, the two DyPs possessed similar apparent specificities (k_{cat}/K_m) for ABTS. However, they had very different apparent specificities for the other reductive substrates (Table 2). Thus, DypA utilized the substrates in the order RB4 > ABTS > pyrogallol and did not detectably oxidize Mn^{II}. By contrast, DypB utilized the substrates in the order ABTS > pyrogallol > RB4 > Mn^{II}. In the presence of constant concentrations of reducing substrates, the DyPs also exhibited different apparent specificities for H_2O_2 (Table 2). More specifically, the apparent specificity of DypB for H_2O_2 was relatively low in the presence of RB4, and that of DypA was relatively low in the presence of ABTS and pyrogallol. Inspection of the steady-state data further revealed that DypA was not saturated for H_2O_2 under the conditions used to study ABTS and pyrogallol oxidation. Attempts to perform studies at higher concentrations of H_2O_2 were confounded by nonenzymatic reactions.

Formation of High-Valent Intermediates upon Reaction with H_2O_2. To investigate the nature of intermediates formed during catalytic turnover of the DyPs, we mixed each with H_2O_2 and recorded the spectra. Adding 1 equiv of H_2O_2 to DypA at pH 7.5 yielded a species with a red-shifted, hypochromatic Soret band at 419 nm and α and β bands at 557 and 528 nm, respectively (Figure 1A, dotted line). These spectral features

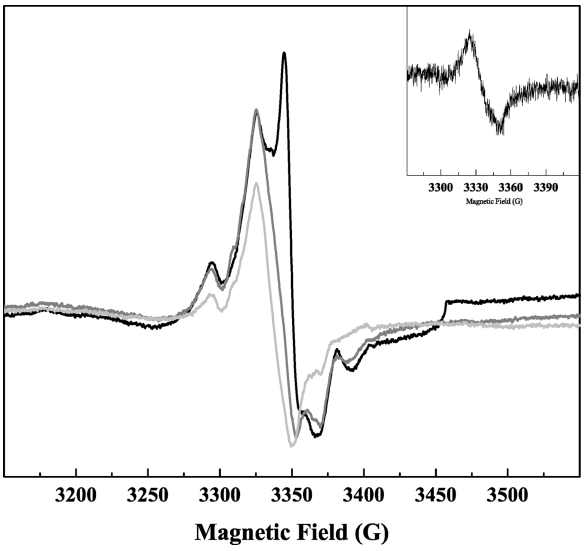

Figure 3. Temperature dependence of the organic radical observed in DypB after reaction with H_2O_2. The 9 GHz EPR spectra were recorded at 5 K (black), 10 K (gray), and 20 K (light gray). The inset shows the spectrum of the same sample recorded at 40 K using using nonsaturating conditions. The signal was centered at $g = 2$.

are consistent with those reported for an $[Fe^{IV}{=}O]$ (compound II)-type species.[43] Under similar conditions, DypB yielded a species with a blue-shifted, hypochromatic Soret band at 397 nm, a prominent shoulder around 340 nm, and bands at 580, 613, and 648 nm overlaying a broad hyperchromaticity between 540 and 700 nm (Figure 1B, dotted line). This spectrum resembled that of a reported $[Fe^{IV}{=}O\ Por^{+}]^{\bullet}$ species in other DyPs[1,2] and had a half-life of ~9 min at 25 °C.

The nature of the high-valent species formed upon reaction of DypB with H_2O_2 was further investigated using EPR spectroscopy. A mixture of 2 mM H_2O_2 with 100 μM DypB for ~2 s on ice turned to a green color enzyme−substrate complex whose EPR spectrum yielded a broad (~250 G) isolated asymmetrical radical with unresolved hyperfine couplings that appeared to be centered at $g = 2.005$ (Figure 2C, 5 K). The g_6 resonance of the ferric enzyme was absent; however, the $g_{\perp} \sim 3.27$ resonance assigned to Π-cation porphyrin radicals was also not observed. The hyperfine structure of this spectrum was strongly temperature-dependent (Figure 3). At 10 K (gray), the $g = 2.0045$ resonance was no longer detectable. At 20 K (light gray), the remaining features were much less intense and were barely detectable at 30 K. In addition, the spectrum of the same sample at 40 K (Figure 3, inset), recorded using nonsaturating conditions, showed little contribution from noncoupled organic radical(s).

Rate of Formation of Compound I. The rate of formation of compound I in DypB was investigated using a stopped-flow reaction analyzer. At pH 7.5, rapid mixing of DypB with H_2O_2 to final concentrations of 5 and 100 μM resulted in decay of the Soret band at 404 nm within ~100 ms with the concomitant appearance of bands characteristic of compound I (Figure 4A). Reactions monitored at 404 and 649 nm for the decay of ferric DypB and formation of compound I, respectively, could be described by a single-exponential equation with similar k_{obs} values (Figure 4C,D). The second-order rate constants, calculated under pseudo-first-order conditions at different H_2O_2 concentrations, k_1, were $(1.79 \pm 0.06) \times 10^5$ and $(1.89 \pm 0.07) \times 10^5\ M^{-1}\ s^{-1}$ at 404 and 649 nm, respectively (Figure 4E,F). Consistent with the similar rate constants and the isosbestic points observed in the scans, no intermediate was resolved using SVD and a two-step model, A → B, fit the data (Figure S3 of the Supporting Information, left panel).

To facilitate comparison with the steady-state studies, transition-state kinetics were repeated using 50 mM acetate (pH 4.5). The results were remarkably similar to those obtained at pH 7.5 (Figure S4 of the Supporting Information, left panel). Thus, the spectrum of compound I was similar except that it was not as hypochromatic as that at pH 7.5 (Figure 4A). Moreover, the calculated second-order rate constants were comparable: $(2.12 \pm 0.01) \times 10^5\ M^{-1}\ s^{-1}$ at 404 nm and $(2.00 \pm 0.07) \times 10^5\ M^{-1}\ s^{-1}$ at 649 nm.

Finally, in reactions performed using a >100-fold excess of H_2O_2, compound I was observed to transform into a second species in ~50 s (Figure 4B). The spectrum of this species resembled that of compound III, an $[Fe^{II}{-}O_2]$ species, with a Soret band at 410 nm and α and β bands at 581 and 543 nm, respectively. Nevertheless, the overall spectral features suggested the presence of more than one intermediate. In these reactions, a three-step model, A → B → C, could be fitted to the data (Figure S3 of the Supporting Information, right panel). At pH 7.5 using 100 equiv of H_2O_2, the transition rate for the decay of compound I to compound II (B → C) was $(8.0 \pm 0.1) \times 10^{-3}\ s^{-1}$.

DypB Structure. The native DypB structure was initially determined and refined to 2.1 Å resolution from a crystal in space group $P3_221$ (Table 1). Subsequently, crystals were obtained in space group $R32$ that improved the resolution to 1.4 Å, and the corresponding structure was used for all analyses herein. DypB consists of two similar domains, each containing a four-strand, antiparallel β-sheet and peripheral α-helices in a ferredoxin-like fold (Figure 5A) similar to those of chlorite dismutase[44] and DyP_{Dec1}.[3] Of the 350 residues in DypB, 174 residues form 9 α-helices and 15 β-strands. The tertiary structure of DypB is structurally homologous with the four DyPs with published structures based on TM scores exceeding 0.75, with rmsd values for all aligned Cα atoms ranging from 3.1 to 3.6 Å.[44,45] The amino acid sequence identities of each of these DyPs with DypB and their PDB entries are as follows: 13% and 2Y4E for EfeB, 9% and 2D3Q for DyP, 23% and 2IIZ for TyrA, and 31% and 2GVK for btDyP, respectively.

Heme is bound within the C-terminal domain of DypB (Figure 5A). His226, conserved in DyPs, acts as the proximal ligand, with an Nε2−iron distance of 2.0 Å (Figure 5B). The carboxylate of another conserved residue, Asp228, forms a hydrogen bond with His226 Nδ1 (2.6 Å). The sixth coordinate position of the heme iron is occupied by a solvent species, 2.1 Å from the iron. The distal face of the heme interacts with three residues of note: Asp153 and Arg244, which are conserved in DyPs, and Asn246, which is not. Asp153 Oδ1 and Asn246 Nδ2 are both within hydrogen bonding distance of the iron-bound solvent species, 3.5 and 3.1 Å, respectively. However, the Asn246 side chain is modeled in two conformations, and the Nδ2 atom has a B factor of ~24 Å^2, significantly greater than those of the heme atoms (average B factor of 11 Å^2), reflecting its flexibility in the structure (Figure 5B). The third residue on the distal face of the heme, Arg244, forms a hydrogen bond (2.8 Å) with the distally positioned heme propionate-A via Nη1.

Although the heme is largely located within the protein matrix, access to solvent is provided by two features: a distal channel and a propionate pocket. The channel is ~19 Å long, is lined

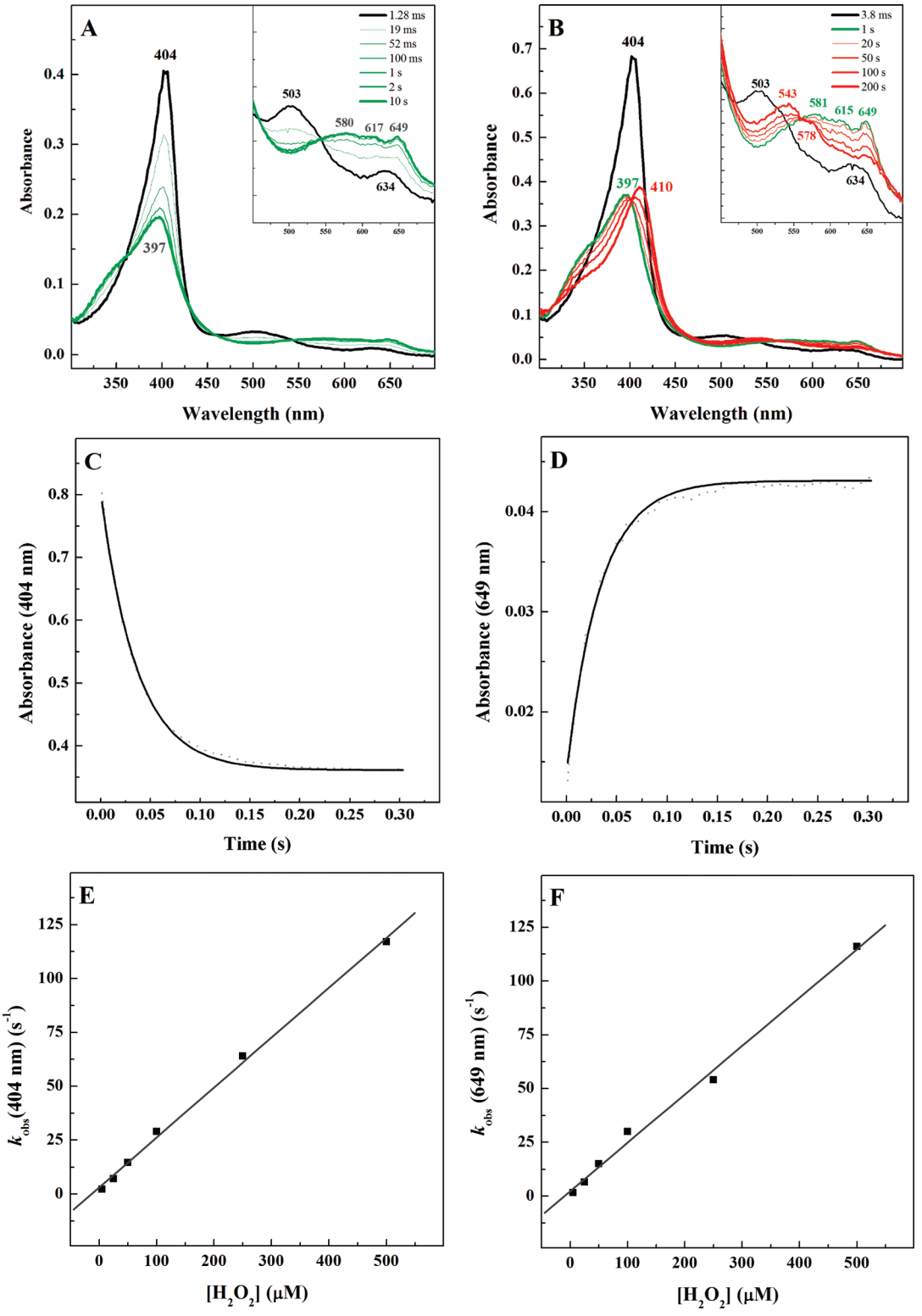

Figure 4. Stopped-flow analyses of the reaction of DypB with H_2O_2 [20 mM MOPS and 80 mM NaCl (pH 7.5, 25 °C)]. (A) Reaction of 5 μM DypB with 100 μM H_2O_2 (final concentrations). (B) Reaction of 5 μM DypB with 500 μM H_2O_2. The black traces, recorded immediately after mixing, correspond to the spectra of the ferric enzyme. The transitions to the first and second intermediates are colored green and red, respectively. (C and D) Reaction traces of 5 μM DypB with 100 μM H_2O_2 recorded at (C) 404 and (D) 649 nm. Solid curves represent fits of single-exponential decays to the data. (E and F) Plots of k_{obs} vs H_2O_2 concentration to determine second-order rate constants at (E) 404 and (F) 649 nm.

predominantly by polar and charged residues, and leads to the distal face of the heme (Figure 6A). The channel entrance is formed, in part, by Ser145 and Arg141. The propionate pocket includes both heme propionates and several bound water

dx.doi.org/10.1021/bi200427h |*Biochemistry* 2011, 50, 5108–5119

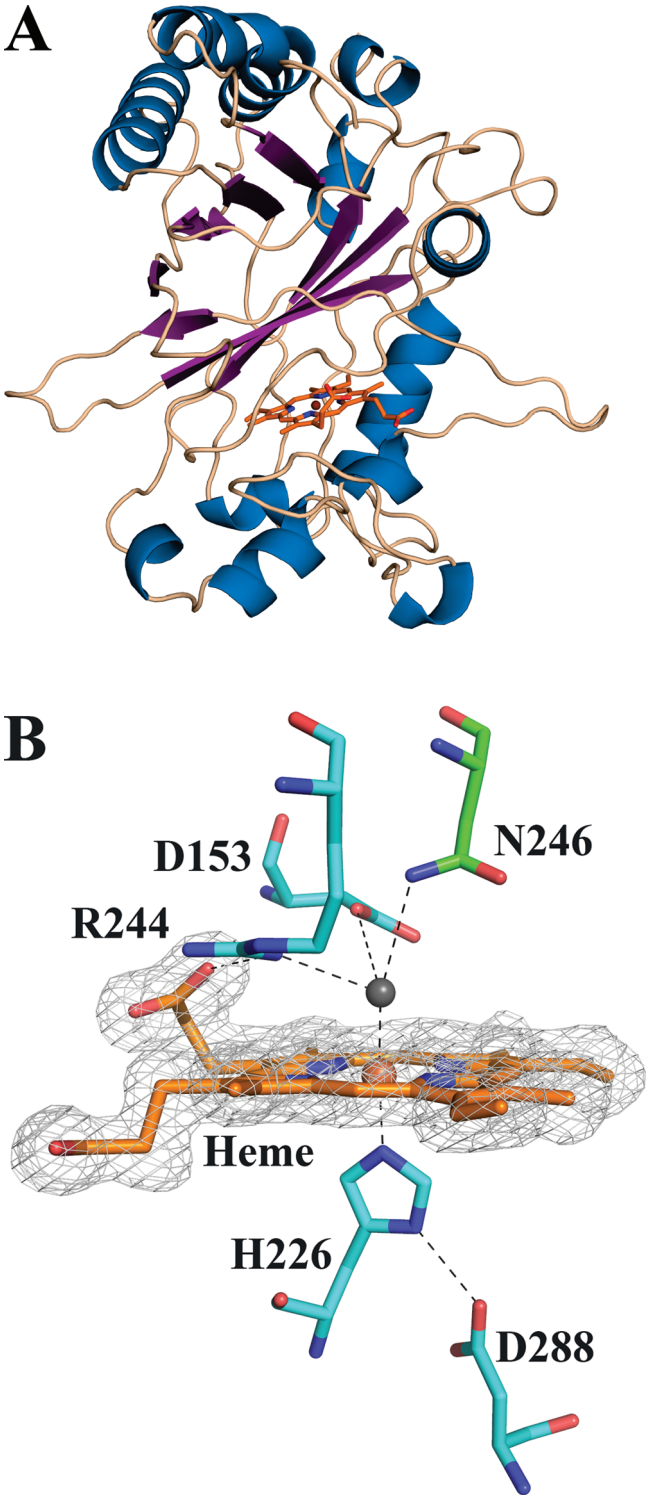

Figure 5. Structure of DypB from *R. jostii* RHA1. (A) Structure of the DypB protomer. α-Helices, β-sheets, and loops are colored blue, violet, and wheat, respectively. The heme prosthetic group is shown as a stick model with carbon atoms colored orange. Nitrogen, oxygen, and iron atoms are colored blue, red, and brown, respectively. (B) Model of the DypB active site. The omit difference ($F_o - F_c$) electron density (contour level of 3σ) for the heme molecule is shown as a gray mesh. The water molecule is colored dark gray, and residues are colored cyan and green for residues conserved among all DyPs and conserved among a subset of B-type DyPs, respectively. Key noncovalent bonds are represented as dashed lines. Only one of the modeled conformations of Asn246 is indicated.

molecules (Figure 6B). It is lined by the side chains of Asp156, Arg208, Glu215, and Glu239, the first three of which are conserved in B-type DyPs. Specifically, the propionate-A of the heme forms a 2.9 Å hydrogen bond to the backbone amide of Asp156 and a 2.7 Å hydrogen bond with water420, which is in turn within H-bonding distance of Arg208 Nη1. The propionate-D forms hydrogen bonds to water561 and water473, both at distances of 2.7 Å, which in turn form hydrogen bonds to the side chain amides of Asn215 and Asn239 at the molecular surface. Comparison with the available homologous structures suggests that the propionate pocket is conserved while the distal channel is found in B- and D-type DyPs, but not A-type DyPs (Figure S5 of the Supporting Information). Moreover, the residues lining the distal channel are not particularly well conserved. Thus, Arg141 is conserved in B-type DyPs, with one exception in which this position is substituted with Val. Similarly, Asp245 is not conserved in B-type DyPs. Interestingly, Arg occurs at this position in the A- and D-type enzymes.

Because DypB oxidizes Mn^{II} in the presence of H_2O_2, the structure of DypB was analyzed for potential Mn^{II}-binding sites using the CHED algorithm[46] and low-stringency filters. A potential site was identified within the propionate pocket defined above and is predicted to be comprised of three acidic residues: Glu156, Glu239, and propionate-D (Figure 6B). Replacing water561 within the hydrogen bonding network of the propionate pocket with Mn^{II} would allow the latter to coordinate with the three aforementioned carboxylates. Two other carboxylates are also in this vicinity: those of residues Asp241 and Glu215. The proximity of the putative Mn^{II} site to the heme is within range for electron transfer. Of these residues, only Glu156 and Glu215 are conserved to any extent among DyPs, and even then only in the B-type DyPs.

Finally, the DypB structure was inspected for potential binding sites for substrates such as Kraft lignin, which shows saturation kinetics with DypB. We identified a hydrophobic groove at the protein surface consisting of Pro93, Val94, His95, Phe279, and Tyr287 that could be involved in binding and long-range electron transfer from a hydrophobic substrate through Tyr287 and Asp288, which forms a hydrogen bond with His226, the fifth ligand to the heme iron.

DISCUSSION

The preceding paper (DOI 10.1021/bi101892z) establishes that RHA1 contains A- and B-type DyP peroxidases, the latter of which is involved in the bacterium's lignin-transforming activity. The current characterization suggests that DyPs are not as catalytically efficient as plant-type peroxidases and that there are significant subfamily-dependent differences in both the peroxidase activities and heme environments of DyPs. Thus, while electronic absorption and EPR spectra indicate that both DypA and DypB contain predominantly high-spin, pentacoordinated heme in the resting state, the spectroscopic data also indicate that the respective iron coordination environments are distinct in the two paralogues. Interestingly, the crystallographic structure of DypB reveals a hexacoordinated heme iron with histidine and a solvent species, 2.12 Å from the Fe atom, occupying axial positions. Further experiments are required to determine the reason for the discrepancy in the spectroscopic and crystallographic data, which may be due to photoreduction of the heme by the X-ray beam during data collection or the crystallization conditions. Differences in the specificity of the two DyPs for various electron donors and H_2O_2 are highlighted by

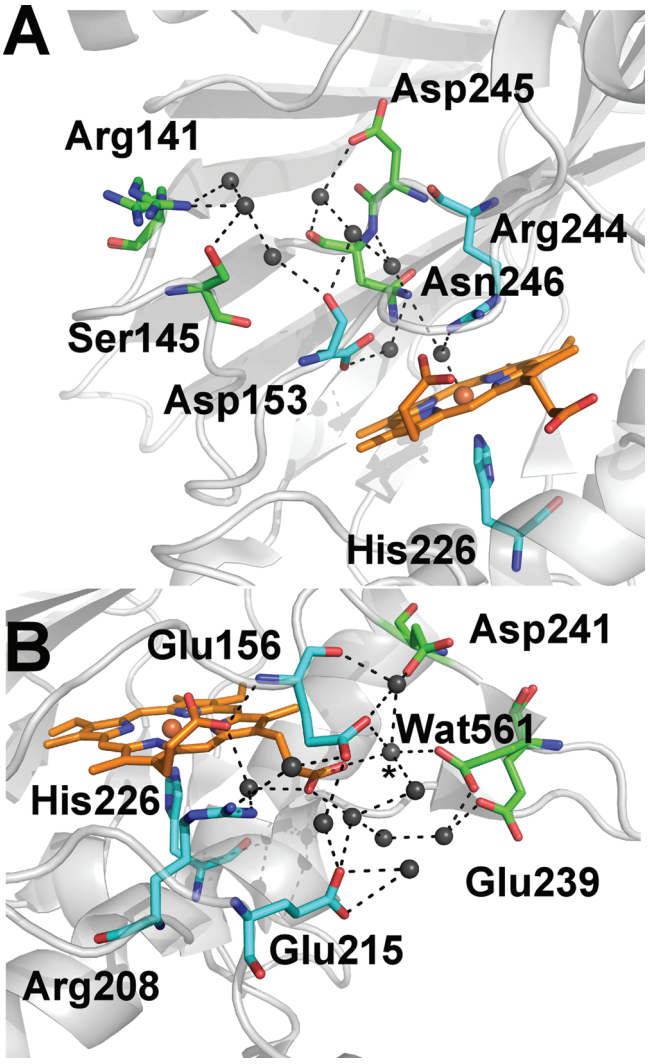

Figure 6. Solvent accessibility of the heme in DypB from *R. jostii* RHA1. (A) Distal channel providing solvent access to the distal heme face. Atoms are colored as in Figure 5B, and the protein backbone is shown as a light gray, semitransparent cartoon. (B) Shallow pocket providing solvent access to the heme propionates. The hydrogen bonds are represented as black dashed lines. Atoms are colored as in panel A. The water molecule bound at the proposed Mn^{II}-binding site is highlighted with an asterisk.

the relatively poor reactivity of DypB with RB4, an AQ dye, as well as this enzyme's ability to oxidize Mn^{II}. Moreover, reaction of the two proteins with H_2O_2 resulted in different intermediates: the DypA intermediate had a spectrum similar to that of compound II in horseradish peroxidase (HRP), consistent with an Fe^{IV}═O species, while the relatively stable DypB intermediate had an electronic absorption spectrum similar to that of compound I of HRP (Table S1 of the Supporting Information). However, the EPR spectrum of the DypB intermediate is not consistent with an $[Fe^{IV}$═O $Por^{+}]^{\bullet}$ species. As discussed below, the structure of DypB provides a number of clues regarding its relative reactivity with H_2O_2 and Mn^{II}.

Comparison of the steady-state kinetic data of DypA and DypB with the available data reveals potential subfamily-dependent differences in the peroxidase activities of DyPs. First, not all DyPs preferentially utilize AQ dyes as reducing substrates despite their namesake.[1,2,4,5,8,47] This is particularly striking for DypB, which has a relatively low specificity for RB4. Second, the C- and D-type DyPs have much higher peroxidase activities than the A- and B-type enzymes. With respect to AQ dyes, the C- and D-type DyPs have specificity constants that are up to 4 orders of magnitude higher (Table S2 of the Supporting Information). A more general comparison involving other reducing substrates indicates that among characterized DyPs, only the D-type enzymes AjPI and AjPII[5] transform reductive substrates and H_2O_2 as efficiently as plant-type peroxidases (Table S3 of the Supporting Information). The RHA1 isozymes are more typical of DyPs in that their substrate specificities are from ~10- to ~10^4-fold lower than those of plant-type peroxidases. Similarly, the apparent k_{cat} of the RHA1 DyPs is up to 3 orders of magnitude lower than that of plant-type peroxidases (Table S3 of the Supporting Information). Finally, the second-order rate constant for the reaction of H_2O_2 with DypB is ~1 order of magnitude lower than those reported for plant-type peroxidases such as HRP (1.7×10^6 M^{-1} s^{-1}).[43] While it is unclear whether H_2O_2 reacts as slowly in all DyPs, the lower rate constant is consistent with the lower specificity of DyPs for peroxidase substrates.

Structural data provide insight into the different specificities of DyPs. Thus, the structure of DypB suggests two access routes to the heme: the distal channel (Figure 6A) and the propionate pocket (Figure 6B). In DypB, the distal channel provides the only continuous pathway from the bulk solvent to the heme iron and is lined with hydrophilic residues, suggesting that it might provide access for H_2O_2. The distal channel is wider in DyP_{Dec1}[48−50] than in DypB (Figure S5 of the Supporting Information) and is blocked in the A-type EfeB (PDB entry 2Y4E),[51] the DyP of known structure sharing the highest amino acid sequence identity with DypA at 27%. It is unclear whether the channel remains blocked in EfeB throughout the catalytic cycle. Nevertheless, the width of the channel correlates with the reactivity of DyPs with H_2O_2: DyP_{Dec1} is a much more efficient peroxidase than DypB, while DypA is poorer, as discussed above. HRP also has a similar access channel to the distal side of the heme (Figure S5 of the Supporting Information). Consistent with HRP's higher catalytic efficiency, this channel is significantly wider than those of the characterized DyPs. The distal channel has been proposed to provide access of AQ dyes to the heme of DyP_{Dec1} based on substrate docking experiments.[4] In DypB, the channel is not wide enough to provide access for organic substrates to the heme. Given that DypA and DypB have similar specificity constants for RB4, it is possible that reducing substrates access the heme via an alternate route in these enzymes, such as the propionate pocket.

The structural data also provide a rationale for the different reactivities of the rhodococcal DyPs and MnP with Mn^{II}. Thus, the constellation of acidic residues in the propionate pocket of DypB is predicted to provide a low-affinity binding site for Mn^{II} appropriately positioned for electron transfer with the heme (Figure 6B). Consistent with DypA's lack of Mn^{II} oxidizing activity, the predicted Mn^{II}-binding residues are unique to DypB according to the crystal structures and amino acid sequences available for DyPs. Similarly, the Mn^{II} binding site of MnP from *Phanerochaete chrysoporium*[52] comprises six carboxylates, twice the number of the predicted site in DypB. The predicted lower affinity of DypB for Mn^{II} versus that of bona fide Mn-peroxidases is consistent with DypB's lower reactivity with Mn^{II}. More particularly, the apparent k_{cat}/K_m of DypB for Mn^{II} is ~10^4−10^5-fold lower than those of the MnPs from *P. chrysosporium*,[53] *Panus tigrinus*,[54] and *Bjerkandera* sp. BOS55.[55] Further studies are being

performed to establish the role of the DypB residues in Mn^{II} binding and to improve the affinity of DypB for Mn^{II}.

Our spectroscopic data clearly indicate that while both RHA1 DyPs contain high-spin Fe^{III} in the resting state, their respective heme iron coordination environments are different. Thus, the Soret band in the electronic absorption spectra is 4 nm blue-shifted and 50% less intense in DypB than in DypA. Similarly, the EPR signal of DypA is more rhombic, indicative of a different heme iron coordination environment.[56,57] Comparison with other DyPs is hindered by a lack of data: most studies have utilized preparations with very low *Rz* values, and none have provided EPR spectra. Nevertheless, A-type YcdB from *E. coli* has a Soret band at 406 nm with weak features at 485 and 660 nm,[15] while another A-type enzyme, TfuDyP of *Thermobifida fusca*, has a Soret band at 409 nm and bands at 540 and 575 nm.[8] Finally, DyP_{Dec1} has a Soret band at 406 nm with bands at 506 and 636 nm.[8] It is unclear whether these differences reflect differences in preparations or the heme iron coordination environment in the different classes of DyPs. The structure of DypB combined with sequence data and the recent structure of the A-type EfeB of *E. coli*[51] indicate that most of the heme pocket residues of DypB are conserved in DypA, including the histidine ligand as well as the aspartate and arginine residues on the distal face of the heme. The notable exception is Asn246, which may form a hydrogen bond with the solvent species coordinated to the heme iron in DypB: this residue is glycine in DypA. Further studies are required to determine the roles of the distal residues in modulating the electronic structure of the heme in these enzymes.

The nature of the relatively stable, green-colored intermediate formed upon the reaction of DypB with H_2O_2 is unclear. The absorption spectrum of this intermediate (Figure 1) is very similar to what has been reported for Dyp_{Dec1},[3,48−50] which in turn was identified as an $[Fe^{IV}{=}O\ Por^{+}]^{\bullet}$ species on the basis of its similarity with compound I of HRP.[43] Moreover, the DypB intermediate has an organic radical, as indicated by the $g = 2$ signal in its EPR spectrum (Figure 2). However, the hyperfine structure of this signal differs from what has been reported for $[Fe^{IV}{=}O\ Por^{+}]^{\bullet}$,[48−50] and the spectrum lacks the axial $g_{\perp} = 3.27$ resonance that characterizes the π-cation porphyrin radical of HRP[58] and lignin peroxidase.[49] The hyperfine structure of the radical also differs from what has been reported in cytochrome *c* peroxidase (CcP)[59] and KatG.[56,60] In the latter cases, an axial **g** tensor with effective values of $g_{\perp} = 2.01$ and $g_{\parallel} = 2.04$ has been assigned to a tryptophan radical, $Trp^{\bullet}$, weakly coupled to the oxoferryl moiety. While the exact nature of the radical in DypB remains unclear, the relaxation properties of the hyperfine structure at temperatures above 5 K (Figure 3) suggest that it is only weakly coupled to the ferryl-iron center. Moreover, the spectrum recorded at 40 K showed little contribution from noncoupled protein radical(s). Further studies are required to elucidate the nature of the long-lived, green-colored DypB intermediate and whether this is the first species formed upon reaction between DypB and H_2O_2.

Catalytic roles for the distal aspartate and arginine have been proposed on the basis of structural and mutagenesis studies.[2,3] Asp153 (DypB with RHA1 numbering) has been proposed to act as a proton shuttle in the formation of compound I from H_2O_2 on the basis of its similarity to the distal Glu of CPO, while Arg244 has been proposed to stabilize the negative charge during the heterolytic cleavage of the peroxide group, as in plant-type peroxidases.[17] However, neither proposed role has been experimentally validated, and substitution of the aspartate in A-type EfeB had a relatively weak effect on the enzyme's peroxidase activity.[51] Indeed, DyPs must stabilize the compound I intermediate differently than CPO as the latter has a cysteinyl proximal ligand, a histidine that modulates the distal glutamate,[61] and no distal arginine. The finding that DypA stabilizes different intermediates suggests the catalytic cycle involves residues other than the conserved aspartate and arginine. In DypB, such a residue could be Asn246, whose Nδ2 atom is 3.1 Å from the solvent species coordinated with the heme iron (Figure 5B), closer than Asp153 Oδ1. Asn246 is also part of the distal solvent access channel, further suggesting that it could mediate the accessibility of H_2O_2 to the heme iron. Finally, the equivalent position in DypA, which forms a compound II-like intermediate upon reaction with H_2O_2, is glycine. Plant-type peroxidases also contain a distal asparagine that is hydrogen bonded to the catalytic histidine. However, as exemplified by Asn70 in HRP[62] and Asn153 in *Synechocystis* KatG,[63] the asparagine is not in direct contact with the solvent species ligated to the heme iron. Further work is required to elucidate the structural basis for the peroxidative cycle in DyPs and the unusual stability of the compound I-like intermediate in B- and D-type DyPs.

Contrary to their nomenclature, the DyPs are emerging as a class of diverse enzymes. Although their physiological roles remain ill-defined, they have been implicated in oxidative stress[10] and deferrochelation.[12] While it is possible that the peroxidase activity of some of the DyP enzymes is not relevant to their physiological roles, their biotechnological applications include lignin degradation (DOI 10.1021/bi101892z) in addition to dye decolorization. Additional studies of DyPs from different subfamilies are warranted to determine their physiological roles as well as the structural basis for their various activities.

■ ASSOCIATED CONTENT

Supporting Information. Additional absorption spectra discussed in the text, comparison of published DyP and plant peroxidase steady-state kinetic parameters, structure-based alignment of DyP sequences, and data used to evaluate the molecular weight of the DyPs. This material is available free of charge via the Internet at http://pubs.acs.org.

■ AUTHOR INFORMATION

Corresponding Author

*Address: 2350 Health Sciences Mall, Vancouver, British Columbia V6T 1Z3, Canada. Telephone: (604) 822-0042. Fax: (604) 822-6041. E-mail: leltis@interchange.ubc.ca.

Author Contributions

J.N.R. and R.S. contributed equally to this work.

Funding Sources

J.N.R. is a recipient of a studentship from the National Science and Engineering Research Council (NSERC) of Canada. J.C.G. was the recipient of an NSERC Graduate Scholarship and a Michael Smith Institute for Health Research Junior Graduate Student Trainee Award. This work was supported by NSERC Discovery Grants (to L.D.E. and M.E.P.M.) and a research grant from the BBSRC IBTI Biorefinery Club (to T.D.H.B.).

■ ACKNOWLEDGMENT

Portions of this research were conducted at the Stanford Synchrotron Radiation Lightsource (SSRL) and the Canadian Light Source (CLS). The SSRL is a Directorate of the SLAC

National Accelerator Laboratory and an Office of Science User Facility operated for the U.S. Department of Energy (DOE) Office of Science by Stanford University. The SSRL Structural Molecular Biology Program is supported by the DOE Office of Biological and Environmental Research and by the National Institutes of Health, National Center for Research Resources, Biomedical Technology Program (P41RR001209), and the National Institute of General Medical Sciences. The CLS is supported by NSERC, the National Research Council Canada, the Canadian Institutes of Health Research, the Province of Saskatchewan, Western Economic Diversification Canada, and the University of Saskatchewan. We thank Drs. Grant Mauk and Pierre Kennepohl for providing access to their EPR spectrometers and Jie Liu for providing expert molecular biology advice.

■ ABBREVIATIONS

DyP, dye-decolorizing peroxidase; AQ, anthraquinone; ABTS, 2,2′-azinobis(3-ethylbenzthiazoline-6-sulfonic acid); CPO, chloroperoxidase; TAT, twin arginine transport; rmsd, positional root-mean-square deviation; RB4, Reactive Blue 4; SVD, singular-value decomposition; PDB, Protein Data Bank.

■ REFERENCES

(1) Kim, S. J., and Shoda, M. (1999) Purification and characterization of a novel peroxidase from *Geotrichum candidum* Dec 1 involved in decolorization of dyes. *Appl. Environ. Microbiol. 65*, 1029–1035.

(2) Sugano, Y. (2009) DyP-type peroxidases comprise a novel heme peroxidase family. *Cell. Mol. Life Sci. 66*, 1387–1403.

(3) Sugano, Y., Muramatsu, R., Ichiyanagi, A., Sato, T., and Shoda, M. (2007) DyP, a unique dye-decolorizing peroxidase, represents a novel heme peroxidase family: ASP171 replaces the distal histidine of classical peroxidases. *J. Biol. Chem. 282*, 36652–36658.

(4) Ogola, H. J. O., Kamiike, T., Hashimoto, N., Ashida, H., Ishikawa, T., Shibata, H., and Sawa, Y. (2009) Molecular Characterization of a Novel Peroxidase from the Cyanobacterium *Anabaena* sp. Strain PCC 7120. *Appl. Environ. Microbiol. 75*, 7509–7518.

(5) Liers, C., Bobeth, C., Pecyna, M., Ullrich, R., and Hofrichter, M. (2010) DyP-like peroxidases of the jelly fungus *Auricularia auricula-judae* oxidize nonphenolic lignin model compounds and high-redox potential dyes. *Appl. Microbiol. Biotechnol. 85*, 1869–1879.

(6) Sugano, Y., Sasaki, K., and Shoda, M. (1999) cDNA cloning and genetic analysis of a novel decolorizing enzyme, peroxidase gene dyp from *Geotrichum candidum* Dec 1. *J. Biosci. Bioeng. 87*, 411–417.

(7) Sugano, Y., Matsushima, Y., Tsuchiya, K., Aoki, H., Hirai, M., and Shoda, M. (2009) Degradation pathway of an anthraquinone dye catalyzed by a unique peroxidase DyP from *Thanatephorus cucumeris* Dec 1. *Biodegradation 20*, 433–440.

(8) van Bloois, E., Pazmino, D. E. T., Winter, R. T., and Fraaije, M. W. (2010) A robust and extracellular heme-containing peroxidase from *Thermobifida fusca* as prototype of a bacterial peroxidase superfamily. *Appl. Microbiol. Biotechnol. 86*, 1419–1430.

(9) Zelena, K., Zorn, H., Nimtz, M., and Berger, R. G. (2009) Heterologous expression of the msp2 gene from *Marasmius scorodonius*. *Arch. Microbiol. 191*, 397–402.

(10) Kaur, A., Van, P. T., Busch, C. R., Robinson, C. K., Pan, M., Pang, W. L., Reiss, D. J., Diruggiero, J., and Baliga, N. S. (2010) Coordination of frontline defense mechanisms under severe oxidative stress. *Mol. Syst. Biol. 6*, 393.

(11) Kong, L., Guo, D., Zhou, S., Yu, X., Hou, G., Li, R., and Zhao, B. (2010) Cloning and expression of a toxin gene from *Pseudomonas fluorescens* GcM5−1A. *Arch. Microbiol. 192*, 585–593.

(12) Letoffe, S., Heuck, G., Delepelaire, P., Lange, N., and Wandersman, C. (2009) Bacteria capture iron from heme by keeping tetrapyrrol skeleton intact. *Proc. Natl. Acad. Sci. U.S.A. 106*, 11719–11724.

(13) Sutter, M., Boehringer, D., Gutmann, S., Gunther, S., Prangishvili, D., Loessner, M. J., Stetter, K. O., Weber-Ban, E., and Ban, N. (2008) Structural basis of enzyme encapsulation into a bacterial nanocompartment. *Nat. Struct. Mol. Biol. 15*, 939–947.

(14) Ogola, H. J., Hashimoto, N., Miyabe, S., Ashida, H., Ishikawa, T., Shibata, H., and Sawa, Y. (2010) Enhancement of hydrogen peroxide stability of a novel *Anabaena* sp. DyP-type peroxidase by site-directed mutagenesis of methionine residues. *Appl. Microbiol. Biotechnol. 87*, 1727–1736.

(15) Sturm, A., Schierhorn, A., Lindenstrauss, U., Lilie, H., and Bruser, T. (2006) YcdB from *Escherichia coli* reveals a novel class of TAT-dependently translocated hemoproteins. *J. Biol. Chem. 281*, 13972–13978.

(16) Zubieta, C., Joseph, R., Krishna, S. S., McMullan, D., Kapoor, M., Axelrod, H. L., Miller, M. D., Abdubek, P., Acosta, C., Astakhova, T., Carlton, D., Chiu, H. J., Clayton, T., Deller, M. C., Duan, L., Elias, Y., Elsliger, M. A., Feuerhelm, J., Grzechnik, S. K., Hale, J., Han, G. W., Jaroszewski, L., Jin, K. K., Klock, H. E., Knuth, M. W., Kozbial, P., Kumar, A., Marciano, D., Morse, A. T., Murphy, K. D., Nigoghossian, E., Okach, L., Oommachen, S., Reyes, R., Rife, C. L., Schimmel, P., Trout, C. V., van den Bedem, H., Weekes, D., White, A., Xu, Q. P., Hodgson, K. O., Wooley, J., Deacon, A. M., Godzik, A., Lesley, S. A., and Wilson, I. A. (2007) Identification and structural characterization of heme binding in a novel dye-decolorizing peroxidase, TyrA. *Proteins 69*, 234–243.

(17) Poulos, T. L., and Kraut, J. (1980) The stereochemistry of peroxidase catalysis. *J. Biol. Chem. 255*, 8199–8205.

(18) Yam, K. C., Okamoto, S., Roberts, J. N., and Eltis, L. D. (2011) Adventures in *Rhodococcus*: From steroids to explosives. *Can. J. Microbiol. 57*, 155–168.

(19) van der Geize, R., and Dijkhuizen, L. (2004) Harnessing the catabolic diversity of rhodococci for environmental and biotechnological applications. *Curr. Opin. Microbiol. 7*, 255–261.

(20) Seto, M., Masai, E., Ida, M., Hatta, T., Kimbara, K., Fukuda, M., and Yano, K. (1995) Multiple polychlorinated biphenyl transformation systems in the Gram-positive bacterium *Rhodococcus* sp. strain RHA1. *Appl. Environ. Microbiol. 61*, 4510–4513.

(21) McLeod, M. P., Warren, R. L., Hsiao, W. W., Araki, N., Myhre, M., Fernandes, C., Miyazawa, D., Wong, W., Lillquist, A. L., Wang, D., Dosanjh, M., Hara, H., Petrescu, A., Morin, R. D., Yang, G., Stott, J. M., Schein, J. E., Shin, H., Smailus, D., Siddiqui, A. S., Marra, M. A., Jones, S. J., Holt, R., Brinkman, F. S., Miyauchi, K., Fukuda, M., Davies, J. E., Mohn, W. W., and Eltis, L. D. (2006) The complete genome of *Rhodococcus* sp. RHA1 provides insights into a catabolic powerhouse. *Proc. Natl. Acad. Sci. U.S.A. 103*, 15582–15587.

(22) Ahmad, M., Taylor, C. R., Pink, D., Burton, K., Eastwood, D., Bending, G. D., and Bugg, T. D. (2010) Development of novel assays for lignin degradation: Comparative analysis of bacterial and fungal lignin degraders. *Mol. BioSyst. 6*, 815–821.

(23) Falk, J. E. (1964) *Porphyrins and metalloporphyrins; their general, physical and coordination chemistry, and laboratory methods*, Elsevier Publishing Co., Amsterdam.

(24) Childs, R. E., and Bardsley, W. G. (1975) Steady-State Kinetics of Peroxidase with 2,2′-Azino-Di-(3-Ethylbenzthiazoline-6-Sulphonic Acid) as Chromogen. *Biochem. J. 145*, 93–103.

(25) Hiner, A. N. P., Rodriguez-Lopez, J. N., Arnao, M. B., Raven, E. L., Garcia-Canovas, F., and Acosta, M. (2000) Kinetic study of the inactivation of ascorbate peroxidase by hydrogen peroxide. *Biochem. J. 348*, 321–328.

(26) Vickers, T. J., and Fairlamb, A. H. (2004) Trypanothione S-transferase activity in a trypanosomatid ribosomal elongation factor 1B. *J. Biol. Chem. 279*, 27246–27256.

(27) Wariishi, H., Valli, K., and Gold, M. H. (1992) Manganese(II) Oxidation by Manganese Peroxidase from the Basidiomycete Phanerochaete-Chrysosporium: Kinetic Mechanism and Role of Chelators. *J. Biol. Chem. 267*, 23688–23695.

(28) Cornish-Bowden, A. (1995) *Analysis of enzyme kinetic data*, Oxford University Press, Oxford, U.K.

(29) Van Duyne, G. D., Standaert, R. F., Karplus, P. A., Schreiber, S. L., and Clardy, J. (1993) Atomic structures of the human

immunophilin FKBP-12 complexes with FK506 and rapamycin. *J. Mol. Biol. 229*, 105–124.

(30) Kabsch, W. (2010) XDS. *Acta Crystallogr. D66*, 125–132.

(31) Evans, P. (2006) Scaling and assessment of data quality. *Acta Crystallogr. D62*, 72–82.

(32) Terwilliger, T. C., and Berendzen, J. (1999) Automated MAD and MIR structure solution. *Acta Crystallogr. D55*, 849–861.

(33) Terwilliger, T. C. (2000) Maximum-likelihood density modification. *Acta Crystallogr. D56*, 965–972.

(34) Terwilliger, T. C. (2003) Automated main-chain model building by template matching and iterative fragment extension. *Acta Crystallogr. D59*, 38–44.

(35) Emsley, P., and Cowtan, K. (2004) Coot: Model-building tools for molecular graphics. *Acta Crystallogr. D60*, 2126–2132.

(36) Painter, J., and Merritt, E. A. (2006) Optimal description of a protein structure in terms of multiple groups undergoing TLS motion. *Acta Crystallogr. D62*, 439–450.

(37) Murshudov, G. N., Vagin, A. A., and Dodson, E. J. (1997) Refinement of macromolecular structures by the maximum-likelihood method. *Acta Crystallogr. D53*, 240–255.

(38) Collaborative Computational Project Number 4. (1994) The CCP4 suite: Programs for protein crystallography. *Acta Crystallogr. D50*, 760–763.

(39) Leslie, A. G. W. (1992) *Joint CCP4 and ESFEACMB Newsletter on Protein Crystallography*, Vol. 26.

(40) Vagin, A., and Teplyakov, A. (2010) Molecular replacement with MOLREP. *Acta Crystallogr. D66*, 22–25.

(41) Peisach, J., Blumberg, W. E., Ogawa, S., Rachmilewitz, E. A., and Oltzik, R. (1971) The effects of protein conformation on the heme symmetry in high spin ferric heme proteins as studied by electron paramagnetic resonance. *J. Biol. Chem. 246*, 3342–3355.

(42) Webb, S. M., Dick, G. J., Bargar, J. R., and Tebo, B. M. (2005) Evidence for the presence of Mn(III) intermediates in the bacterial oxidation of Mn(II). *Proc. Natl. Acad. Sci. U.S.A. 102*, 5558–5563.

(43) Dunford, H. B. (1999) *Heme peroxidases*, John Wiley, New York.

(44) de Geus, D. C., Thomassen, E. A., Hagedoorn, P. L., Pannu, N. S., van Duijn, E., and Abrahams, J. P. (2009) Crystal structure of chlorite dismutase, a detoxifying enzyme producing molecular oxygen. *J. Mol. Biol. 387*, 192–206.

(45) Zhang, Y., and Skolnick, J. (2005) TM-align: A protein structure alignment algorithm based on the TM-score. *Nucleic Acids Res. 33*, 2302–2309.

(46) Babor, M., Gerzon, S., Raveh, B., Sobolev, V., and Edelman, M. (2008) Prediction of transition metal-binding sites from apo protein structures. *Proteins 70*, 208–217.

(47) Zubieta, C., Krishna, S. S., Kapoor, M., Kozbial, P., McMullan, D., Axelrod, H. L., Miller, M. D., Abdubek, P., Ambing, E., Astakhova, T., Carlton, D., Chiu, H. J., Clayton, T., Deller, M. C., Duan, L., Elsliger, M. A., Feuerhelm, J., Grzechnik, S. K., Hale, J., Hampton, E., Han, G. W., Jaroszewski, L., Jin, K. K., Klock, H. E., Knuth, M. W., Kumar, A., Marciano, D., Morse, A. T., Nigoghossian, E., Okach, L., Oommachen, S., Reyes, R., Rife, C. L., Schimmel, P., van den Bedem, H., Weekes, D., White, A., Xu, Q., Hodgson, K. O., Wooley, J., Deacon, A. M., Godzik, A., Lesley, S. A., and Wilson, I. A. (2007) Crystal structures of two novel dye-decolorizing peroxidases reveal a β-barrel fold with a conserved heme-binding motif. *Proteins 69*, 223–233.

(48) Chance, M., Powers, L., Poulos, T., and Chance, B. (1986) Cytochrome c peroxidase compound ES is identical with horseradish peroxide compound I in iron-ligand distances. *Biochemistry 25*, 1266–1270.

(49) Khindaria, A., and Aust, S. D. (1996) EPR detection and characterization of lignin peroxidase porphyrin π-cation radical. *Biochemistry 35*, 13107–13111.

(50) Patterson, W. R., Poulos, T. L., and Goodin, D. B. (1995) Identification of a porphyrin π cation radical in ascorbate peroxidase compound I. *Biochemistry 34*, 4342–4345.

(51) Liu, X., Du, Q., Wang, Z., Zhu, D., Huang, Y., Li, N., Wei, T., Xu, S., and Gu, L. (2011) Crystal structure and biochemical features of EfeB/YcdB from *Escherichia coli* O157: Asp235 plays divergent roles in different enzyme-catalyzed processes. *J. Biol. Chem. 286*, 14922–14931.

(52) Sundaramoorthy, M., Kishi, K., Gold, M. H., and Poulos, T. L. (1994) The crystal structure of manganese peroxidase from *Phanerochaete chrysosporium* at 2.06-Å resolution. *J. Biol. Chem. 269*, 32759–32767.

(53) Kishi, K., Kusters-van Someren, M., Mayfield, M. B., Sun, J., Loehr, T. M., and Gold, M. H. (1996) Characterization of manganese-(II) binding site mutants of manganese peroxidase. *Biochemistry 35*, 8986–8994.

(54) Petruccioli, M., Frasconi, M., Quaratino, D., Covino, S., Favero, G., Mazzei, F., Federici, F., and D'Annibale, A. (2009) Kinetic and redox properties of MnP II, a major manganese peroxidase isoenzyme from *Panus tigrinus* CBS 577.79. *J. Biol. Inorg. Chem. 14*, 1153–1163.

(55) Mester, T., and Field, J. A. (1998) Characterization of a novel manganese peroxidase-lignin peroxidase hybrid isozyme produced by *Bjerkandera* species strain BOS55 in the absence of manganese. *J. Biol. Chem. 273*, 15412–15417.

(56) Ivancich, A., Jakopitsch, C., Auer, M., Un, S., and Obinger, C. (2003) Protein-based radicals in the catalase-peroxidase of *Synechocystis* PCC6803: A multifrequency EPR investigation of wild-type and variants on the environment of the heme active site. *J. Am. Chem. Soc. 125*, 14093–14102.

(57) Carpena, X., Wiseman, B., Deemagarn, T., Singh, R., Switala, J., Ivancich, A., Fita, I., and Loewen, P. C. (2005) A molecular switch and electronic circuit modulate catalase activity in catalase-peroxidases. *EMBO Rep. 6*, 1156–1162.

(58) Ortiz de Montellano, P. R. (1992) Catalytic sites of hemoprotein peroxidases. *Annu. Rev. Pharmacol. Toxicol. 32*, 89–107.

(59) Sivaraja, M., Goodin, D. B., Smith, M., and Hoffman, B. M. (1989) Identification by ENDOR of Trp191 as the free-radical site in cytochrome c peroxidase compound ES. *Science 245*, 738–740.

(60) Singh, R., Switala, J., Loewen, P. C., and Ivancich, A. (2007) Two [Fe(IV)═O Trp^{+}] intermediates in *M. tuberculosis* catalase-peroxidase discriminated by multifrequency (9−285 GHz) EPR spectroscopy: Reactivity toward isoniazid. *J. Am. Chem. Soc. 129*, 15954–15963.

(61) Sundaramoorthy, M., Terner, J., and Poulos, T. L. (1995) The crystal structure of chloroperoxidase: A heme peroxidase−cytochrome P450 functional hybrid. *Structure 3*, 1367–1377.

(62) Nagano, S., Tanaka, M., Ishimori, K., Watanabe, Y., and Morishima, I. (1996) Catalytic roles of the distal site asparagine-histidine couple in peroxidases. *Biochemistry 35*, 14251–14258.

(63) Jakopitsch, C., Auer, M., Regelsberger, G., Jantschko, W., Furtmuller, P. G., Ruker, F., and Obinger, C. (2003) The catalytic role of the distal site asparagine-histidine couple in catalase-peroxidases. *Eur. J. Biochem. 270*, 1006–1013.